



Halving of Swiss glacier volume since 1931 observed from terrestrial image photogrammetry

Erik Schytt Mannerfelt^{1,2}, Amaury Dehecq^{1,2,3}, Romain Hugonnet^{1,2,4}, Elias Hodel^{1,2}, Matthias Huss^{1,2,5}, Andreas Bauder^{1,2}, and Daniel Farinotti^{1,2}

¹Laboratory of Hydraulics, Hydrology and Glaciology (VAW), ETH Zurich, Zurich, Switzerland

²Switzerland Swiss Federal Institute for Forest, Snow and Landscape Research (WSL), Birmensdorf, Switzerland

³Univ. Grenoble Alpes, CNRS, IRD, Grenoble INP, IGE, Grenoble, France

⁴LEGOS, Université de Toulouse, CNES, CNRS, IRD, UPS, F-31400 Toulouse, France

⁵Department of Geosciences, University of Fribourg, Fribourg, Switzerland

Correspondence: Erik S. Mannerfelt (mannerfelt@vaw.baug.ethz.ch), Amaury Dehecq (amaury.dehecq@univ-grenoble-alpes.fr)

Abstract. The monitoring of glaciers in Switzerland has a long tradition, yet glacier changes during the 20th century are only known through sparse observations. Here, we estimate a halving of Swiss glacier volumes between 1931 and 2016 by mapping historical glacier elevation changes at high resolution. Our analysis relies on a terrestrial image archive known as *TerrA*, which covers about 86% of the Swiss glacierised area with 21,703 images acquired during the period 1916–1947 (1931 on average).

5 We developed a semi-automated workflow to generate digital elevation models (DEMs) from these images, resulting in a 45% total glacier coverage. Using the geodetic method, we estimate a Swiss-wide glacier mass balance of -0.52 ± 0.09 m w.e. a⁻¹ between 1931 and 2016. This equates to a $51.5 \pm 6.1\%$ loss in glacier volume. We find that low elevation, high debris cover, and gently sloping glacier termini are conducive to particularly high mass losses. In addition to these glacier-specific, quasi-centennial elevation changes, we present a new inventory of glacier outlines with known timestamps and complete attributes
10 from around 1931. The fragmented spatial coverage and temporal heterogeneity of the *TerrA* archive are the largest sources of uncertainty in our glacier-specific estimates, reaching up to 0.50 m w.e. a⁻¹. We suggest that the high-resolution mapping of historic surface elevations could unlock great potentials also for research fields other than glaciology.

1 Introduction

15 Glaciers are melting rapidly on a global scale, and constraints on regional- to global-scale volume changes since the 2000s are constantly improving (Maurer et al., 2019; Zemp et al., 2019; Shean et al., 2020; Hugonnet et al., 2021). Large-scale changes throughout the 1900s are however still largely unknown. Recently, photogrammetric studies reconstructing glacier surface geometries for the late 19th and early 20th centuries have emerged (Mertes et al., 2017; Midgley and Tonkin, 2017; Girod et al., 2018; Dehecq et al., 2020; Holmlund, 2021), partially revealing large discrepancies when compared to model-based estimates (Holmlund and Holmlund, 2019; Belart et al., 2020; Geyman et al., 2022). For a better understanding of the response of glaciers
20 to a changing climate, more historic data to understand these discrepancies are essential.



Glaciers in Switzerland and the European Alps have experienced net retreat since around 1850, albeit at a fluctuating rate, as seen by glaciological mass balance measurements (GLAMOS, 1881–2020; Vincent et al., 2009; Huss et al., 2015; Beniston et al., 2018; Huss et al., 2021). The climate in the 20th century (Figure 1B+D) was generally unfavourable for glaciers, but mass gains and glacier advances were observed in the 1910s, 1920s, 1980s and 1990s. During the last decades, however, an accelerating mass loss trend is seen (Zemp et al., 2019).

Whilst topographic maps resolving Swiss glaciers have been drawn by the Swiss Federal Office of Topography (swisstopo) since the late 19th century, today's picture of glacier changes during the last century is largely based on a combination of (i) long-term glacier mass balance series extending back until the 1910s (GLAMOS, 1881–2020), (ii) repeated aerial photogrammetry acquired after the 1960s (Bauder et al., 2007), and (iii) model-based reconstructions (e.g. Huss et al., 2008). Such combined reconstructions are available for selected glaciers, and the results have been extrapolated to the regional scale (e.g. Huss, 2012). In this context, it is important to note that since the uncertainties of glaciological mass balance series are cumulative, they can cause large biases if not corrected with geodetic estimates over longer periods (Cox and March, 2004; Thibert et al., 2008; Zemp et al., 2010, 2013). For Switzerland, such corrections have generally been based on mass changes derived from topographic maps before 1960 or from detailed geodetic surveys based on aerial imagery. However, uncertainties in the former datasets are large and sometimes difficult to quantify, especially for the first half of the 20th century. Modern reanalysis of the source material for these early maps, thus, holds great potential for further constraining the magnitude and lower the uncertainty of estimates for past glacier changes.

From the First World War to the late 1940s, large parts of the Swiss Alps were surveyed by means of terrestrial (i.e. ground based) photogrammetry. Engineers of swisstopo took photographs from about 7,000 locations distributed across the country, and measured both the terrain and the photographed position with a phototheodolite (that is an angle-measuring device combined with a measuring camera). These surveys, which produced images that are now stored in what is known as the *TerrA* image archive (see Sec. 2.2), served as the basis for the production of the first national topographic maps with a scale of 1:50,000, as well as a set of military maps in the scale 1:10,000.

Here, we re-process 21,703 terrestrial photographs taken during the *TerrA* surveys by using modern photogrammetric methods, and generate digital elevation models (DEMs) of nearly all glaciers in Switzerland. The images and DEMs refer to the time span between 1916 and 1947 (with a centre year of 1931), and are used to reconstruct the geodetic glacier mass balance from 1931 to 2016 (Figure 1). This is one of the rare regional reconstructions based on digital photogrammetry before the 1950s (e.g. Belart et al., 2020; Geyman et al., 2022), and to the knowledge of the authors, the first of such scope to use terrestrial photographs as the source material.

2 Study site and data

2.1 Study site

According to the latest Swiss Glacier Inventory (SGI2016; Linsbauer et al., 2021), Switzerland presently houses ca. 1,400 glaciers covering 961.4 km² in total. By area, this is about half of all glaciers in the European Alps (RGI, 2017). The Swiss



glaciers currently span an elevation range between 1357 and 4599 m a.s.l., with a median elevation of 2913 m a.s.l. and a mean slope of 28° (Linsbauer et al., 2021). Both the median elevation and the mean slope are higher than the global average, which is of 1308 m a.s.l. and 11° , respectively (RGI, 2017). This relative steepness makes Swiss glaciers particularly suited for reconstructions based on terrestrial photogrammetry, as the steepness allows for favourable incidence angles of the photographs. In this study, we consider all glaciers on Swiss territory as long as suitable photographic material is available from the historic surveys (see below).

60 2.2 The “Terra” terrestrial image archive

The Terra archive consists of 57,385 images in total, covering most of the mountains in Switzerland and were acquired during the first half of the 20th century. According to the images’ approximate viewsheds (produced by swisstopo and distributed together with the images), about 21,703 (38%) of these images cover glaciers.

Images were acquired from high points surrounding the surveyed areas (e.g. summits, ridges, slopes), and stereo acquisition was performed by taking two sets of pictures from locations spaced a few hundred metres apart (Figure 2A). From each location, a panorama of about 4–5 images (Figure 2B) was acquired to increase the viewing angle, with all images being acquired in the same orientation as their stereo-counterparts. About 86% of the glacierised area is covered by at least two images taken from different physical locations, thus setting a constraint to the maximum theoretical coverage of the dataset. The actual coverage will be lower, as the incidence angle (i.e. the difference between the angle of the image and the terrain slope) is often low due to the photographs being taken from the ground. This makes it difficult for feature-matching algorithms to get accurate results, thus lowering the coverage.

The 13 cm×18 cm terrestrial images contained in the Terra archive are scanned by swisstopo at a resolution of $21 \mu\text{m}$, yielding digital images of 53 Mpx. Metadata for every image includes an identifier for which stereo pair it belongs to, the acquisition date, the position, and the viewing direction of the image as determined from field measurements. The photographs used in this study were taken with 21 individual cameras between 1916 and 1947. Most photographs were taken in the 1920s and 1930s, with a median year of 1931 and a standard deviation of 5 years. The cameras were of two different brands called “Wild” and “Zeiss”, which had different focal lengths, image dimensions, and frame appearances (Figure 2C,D).

Within the 2008 “Action Plan for the Preservation of the Spatially Relevant Cultural Heritage of swisstopo”, it was decided to preserve the images in the Terra archive, to scan them all, and to make them available to the public (Ryf and Klöti, 2008; Rickenbacher, 2012). After conceptual preparations, swisstopo started the project in 2013, and announced the release of the dataset in 2018 (swisstopo, 2018). To our knowledge, no scientific publication has used this unique digital dataset to date. The novel use of the imagery proposed here, might thus pave the way for further utilisation of the archive.

2.3 Auxiliary data

Our processing workflow (see Sec. 3) requires a modern DEM as a reference for co-registration, as means of validation, and for calculating surface elevation changes with respect to the DEMs generated from the Terra archive. We use the SwissALTI3D DEM (swisstopo, 2019) for this. This DEM is a 2 m×2 m mosaic of LiDAR (below 2000 m a.s.l.) and digital aerial photography.



Over glaciers, acquisitions range from 2007 to 2018, with a median year of 2016. The reported absolute accuracy of the DEM is between 0.1 m and 3 m, depending on the location.

To exclude areas of possible elevation change over the 85-year period, we mask glaciers, perennial snow fields and lakes. To do so, we use (i) the glacier and snow mask that Freudiger et al. (2018) digitized from the “Siegfried maps” made in 1917–1944, and (ii) the swissTLM3D product to mask natural and artificially dammed lakes (swisstopo, 2020).

The Terra images were previously used for creating the first edition of 1:50,000 topographic maps (the so-called “LK50”) in the alpine region of Switzerland (swisstopo, personal comm. 2021). We use georeferenced scans of these maps to derive glacier outlines for all glaciers, which are proven here to be concurrent with the Terra dataset. To digitize glacier outlines from the LK50 map series (see Sec. 3.1.3 for details), we use glacier outlines from the Swiss Glacier Inventory 1973 (SGI1973; Müller et al., 1976) as a template, and follow the same naming convention for glacier identification. The SGI1973 is based on orthophotographs acquired in 1973, and represents the first accurate and complete mapping of Swiss glaciers.

Glacier outlines corresponding to SwissALTI3D DEM are taken from the SGI2016 (Linsbauer et al., 2021). These are based on detailed cartographic mapping performed on orthophotographs with 0.1 to 0.25 m resolution and acquired during the period 2013-2018 (centre year 2016).

Different types of glacier mass balance data covering large parts of the study period are available from long-term monitoring efforts (GLAMOS, 2021). In particular, we use (1) time series of annual glacier-wide mass balance based on in situ observations, available for about two dozens of glaciers and partly extending back to the first half of the 20th century (Huss et al., 2015, 2021); (2) geodetic mass balances computed by differencing up to 12 DEMs, in turn derived from either topographical maps or aerial photogrammetry (before and after the 1960s, respectively), available for about 50 glaciers at intervals between 3 to 60 years (Bauder et al., 2007; GLAMOS, 2021); (3) modelled time series of annual mass balances covering the period 1900-2021, obtained by updating the results from Huss et al. (2008, 2010a, c), who constrained a distributed daily mass balance model to match the observed glacier mass changes given by (1) and (2); and (4) country-wide, region-specific annual mass balances variations covering the last century, obtained by spatial extrapolation of the observations from (1) and (2), and supported by the modelling of (3) for the period before 1955 (GLAMOS, 2018).

The above data are used for both temporal corrections of the heterogeneous imaging period, and independent validation of the results (see Methods).

3 Methods

In this study, we process 21,703 images semi-autonomously to generate DEMs and measure glacier elevation change between 1931 and 2016. The main steps of the methodology are synthesised in Figure 3, with detailed descriptions being provided in the following subsections. In a nutshell, images and associated metadata are preprocessed first for homogenizing the inputs (Sec. 3.1). Then, DEMs are generated for each stereo-panorama and co-registered to the modern stable ground (Sec. 3.2). In a third step, the so-derived DEMs are subtracted from the swissALTI3D DEM to obtain elevation change maps for the period 1931-2016. A temporal correction is performed to standardize the elevation change rates to said period (Secs. 3.2–3.3.2).



120 Finally, the glacier outlines derived from the digitization of the LK50 map are used for masking the results, and for obtaining average elevation change rates and geodetic mass balances (Sec. 3.4).

3.1 Image and data preprocessing

3.1.1 Fiducial mark detection

We use fiducial marks (small markers on the image frame used as fixed references; red squares in Figure 2C+D) to constrain the
125 centrepoint and internal orientation of the imagery. The positions of the fiducial marks are used to calculate a transformation between the pixel coordinates and physical image coordinates. We search for a similarity transformation (translation, rotation and scaling) which is likely to be introduced during scanning. Every image has four or more fiducial marks along its edges, with a size of about 350 px (~ 7 mm). A theoretical minimum of two fiducial marks need to be identified, but more fiducial marks increase redundancy and allows for exclusion of uncertain marks. We use a semi-automatic model to identify fiducial
130 marks in the 21,703 images processed in the study. To calibrate the model, we manually identify fiducial marks in 3,395 images (~ 162 images per camera). Such a large calibration set was required because the 21 unique cameras in the dataset had slightly or completely different fiducial marks. We then use the manual data to calibrate a model to do the same on the remaining 81% of the image archive. Using template matching to identify the fiducial marks, the model estimates a similarity transform and validates it using the residual differences between the identified fiducial marks and the modelled ones. We use Random
135 Consensus Sampling (RANSAC) to exclude fiducial marks with residuals of more than 10 px (0.21 mm). The model found four and three fiducials filtered as inliers in 56% and 32% of the images, respectively, with a median manual-to-automatic transform root-mean-square (RMS) difference of 8.61 px (0.18 mm). We manually mark the remaining 12% of the images (with fewer than three automatic fiducials) to complement the automatic matches. In seven images, only two fiducials could be identified manually, but they are still used in spite of their higher potential error.

140 The border of each image needs exclusion to not interfere with the automatic image alignment. We create image frame masks by calculating the median intensity of all images of a given instrument (after applying the geometric transformation), and then segment the median image frame using thresholding.

3.1.2 Image position correction

A preliminary analysis of the image metadata revealed spatially correlated biases in the provided image positions. This was
145 observed by calculating the elevation difference between the image position and the SwissALTI3D elevation on stable ground. While this difference is expected to be the height of the tripod (~ 1.2 m; swisstopo, personal comm. 2021), the calculated differences had an absolute bias of 2.66 ± 5.91 (mean \pm standard deviation) after taking the tripod height into account. By sampling slope, aspect and elevation values from the reference DEM at every recorded image position, we estimate the approximate 3D offsets from the image position data to the ground. We then partially correct the systematic component of the biases by aver-
150 aging them in 1 km \times 1 km grids, and subtract the gridded offsets from the 3D positions of the images. This correction reduced the average difference between the DEM and the imaging locations to 0.70 ± 5.18 m.



3.1.3 LK50 map series digitization

We obtain glacier outlines concurrent with the Terra dataset by digitizing the scanned and georeferenced LK50 map series. Digitizing glacier outlines from orthoimages generated in this study was also a theoretical possibility, but spotty image coverage and time constraints led to the search for more efficient approaches. These orthoimages are thus only used to draw outlines for 61 sites, which are in turn used to validate the glacier outlines obtained from the LK50 series (see Sec. 3.5.2). The LK50 maps, made in the 1950s, cover all of Switzerland and are based on the Terra photographs among other data. We manually digitize the glacier outlines of the LK50 maps by modifying the outlines of the Swiss Glacier Inventory 1973 as to fit the LK50 map data. This allows for the SGI1973 metadata to be easily retained, and ensures consistency when including or excluding perennial snowfields as well as when drawing ice-divides. We acknowledge that in this way, there is a potential underestimation of change in the accumulation areas. Indeed, the outlines were only modified where they deviated from the SGI1973 outlines, meaning that minor deviations may have been missed. We assume these potential discrepancies to be accounted for in our uncertainty analysis (Sec. 3.5.2). To reduce subjective error, we draw outlines by one person, and validate by another.

3.2 Photogrammetry and DEM generation

We process the 21,703 images photogrammetrically in Agisoft Metashape version 1.6.5 by dividing the images in subsets, and processing each subset individually (Table 1). One subset consists of every image taken with a certain camera at a certain year, totalling 113 groups, with 192 images each on average. We compute a separate camera model for each subset, as the used cameras might vary in their distortion parameters, depending on their construction and in which year they were used; differences may relate to the photographer, potential damages, and subsequent repairs the camera might have endured during its lifetime.

Within each subset, we align the stereo-panoramas individually using separate camera models. The ones that successfully align are then merged using the same camera model. The stereo-panoramas generally overlap with others in terms of detailed terrain, but the angle difference between extracted features is too large for the builtin feature matcher in Metashape to produce reliable tie points between them. We therefore perform an alignment between all separate overlapping stereo-panoramas within a subset using Iterative Closest Point (ICP) co-registration of dense point clouds that are constructed from each stereo-panorama. We use the ICP algorithm implemented in the *xdem* Python package (version 0.0.5; *xdem* contributors, 2021), using core functionality from the *opencv* suite (OpenCV contributors, 2021). We run the co-registration in areas where the dense clouds overlap, plus a buffer of ± 15 m (chosen qualitatively through trial-and-error), to limit the co-registration to reasonable offsets.

Once the stereo-panoramas are aligned to each other, a new camera model is calculated with a bundle adjustment and new dense clouds are generated for each subset individually. We filter the dense clouds by excluding points with a “confidence” of less than or equal to 2. The confidence is a statistic provided by the Metashape software, but information on how it is calculated is unavailable. After the DEMs are generated from the resultant dense clouds, and after orthoimages are draped on the DEMs, we co-register the DEMs to the SwissALTI3D DEM (Figure 4A+B). This is done by using the same ICP co-



185 registration method as in the previous step, but with the modern DEM as a reference outside of the unstable terrain mask. We
use the ICP transforms to correct the position and rotation of both the DEMs and orthoimages. Finally, elevation change maps
are generated by subtracting the DEMs from the reference SwissALTI3D DEM.

3.3 Post-photogrammetric processing

3.3.1 Temporal correction

190 The imaging period of the TerrA dataset ranges from 1916 to 1947, and is centred around 1931 on glacierized terrain (standard
deviation: 5 years). The period of acquisition for the modern SwissALTI3D DEM ranges from 2007 to 2018, with a median year
of 2016 and standard deviation of 2 years. This temporal spread needs correction for facilitating evaluation and interpretation.

We correct each elevation change map to the centre years 1931 and 2016 based on an annual dataset of observed mass
balance variations that is specified for the major hydrological basins of the Swiss Alps (point "(4)" in Sec. 2.3). Regional
195 anomalies in mass balance from a reference period have been derived by spatially extrapolating all available series acquired
using the direct glaciological method (between 8 and 20 glaciers; Huss et al., 2015; GLAMOS, 1881–2020). Before 1955,
modelled mass balance variations for four glaciers were used (Huss et al., 2008). The difference in cumulative annual mass
balance for the respective region between the reference period of 1931–2016 is compared to the period over which elevation
change is calculated (Equation 1). At the pixel scale, elevation change rates over glacierized areas are multiplied by this factor
200 to obtain the temporally corrected elevation change rate $[\frac{dH}{dt}]_{1931-2016}$:

$$[\frac{dH}{dt}]_{1931-2016} = [\frac{dH}{dt}]_{t_0-t_1} \times \frac{B(2016) - B(1931)}{B(t_1) - B(t_0)}, \quad (1)$$

where t_0 and t_1 are the years of acquisition of the TerrA photograph and the SwissALTI3D DEM, respectively, and $B(t)$ is the
representative cumulative mass balance at year t for the given region.

3.3.2 Mosaicking and interpolation

205 We successfully generate 1,907 elevation change maps, which we mosaic by averaging the temporally corrected elevation
changes estimated at each pixel in a $5\text{ m} \times 5\text{ m}$ grid. We exclude three out of the 1,907 elevation change maps from the mosaic
due to extreme median values ($< -350\text{ m}$ or $> 100\text{ m}$). Regionally, 55% of the total glacier area is missing from the elevation
change mosaic, so an interpolation approach is required (Figure 6). Gaps are spread over the whole glacier extents with no
significant trend in elevation, and we therefore chose to harness hypsometric interpolation approaches.

210 We use a modified version of the regional hypsometric approach (McNabb et al., 2019) where each glacier elevation change
is normalized to its elevation range, i.e. scaling both elevation and elevation change from 0 to 1 for each glacier (Huss et al.,
2010b). More specifically, we use the approach as implemented in *xDEM*. This approach relies on elevation changes estimated at
different elevation bins, and aims at capturing the glacier-wide hypsometric signal. Consequently, the quality of the interpo-
lation deteriorates with decreasing spatial coverage. For our application, we qualitatively choose a threshold of $> 20\%$ coverage



215 (8.9% of all glaciers by area are below this threshold). For glaciers that do not meet this condition, we apply the a simple regional hypsometric approach, in which gaps are replaced by the mean regional value within the same elevation band.

3.4 Glacier-specific and regional elevation change

We estimate glacier-specific elevation changes and geodetic mass balances for each entry of the SGI2016 individually. Then, we aggregate glacier-specific estimates to obtain regional-scale estimates.

220 For each individual glacier, we estimate the mean elevation change $\frac{dH}{dt}$ by averaging both the observed and interpolated elevation changes that fall within the historic glacier outline:

$$\frac{dH}{dt} = \frac{\sum [\frac{dH}{dt}]_p}{N_p}. \quad (2)$$

Here, $[\frac{dH}{dt}]_p$ is the elevation change rate of a given pixel p , and N_p is the number of pixels within the glacier outline.

We then estimate the mean volume change rate $\frac{dV}{dt}$ by:

225
$$\frac{dV}{dt} = \frac{dH}{dt} \times A_0, \quad (3)$$

where A_0 is the glacier area as given by the historic glacier outline (referring to ca. 1931).

By applying a volume-to-mass conversion factor of $\rho_{\Delta V} = 850 \text{ kg m}^{-3}$ (Huss, 2013), we estimate the specific-glacier mass balance rate \dot{B} using:

$$\dot{B} = \rho_{\Delta V} \times \frac{\frac{dV}{dt}}{(A_0 + A_1)/2}, \quad (4)$$

230 where A_1 is the glacier area as given by the SGI2016.

Similarly, we estimate the total glacier mass change rate \dot{M} from the volume change and the volume-to-mass conversion factor:

$$\dot{M} = \rho_{\Delta V} \times \frac{dV}{dt}. \quad (5)$$

3.5 Uncertainty analysis

235 We identify multiple sources of error that propagate in our estimates of glacier volume and mass change. These sources include stochastic elevation measurement errors, correlated short- and long-range DEM distortions, error in glacier outlines, the temporal correction, hypsometric interpolation, and the volume-to-mass conversion. We consider these sources separately, and combine them into estimates of uncertainty for elevation, volume, and mass change. Throughout the text, uncertainties are presented through a 95% confidence interval.

240 To propagate uncertainties from the scale of pixels to that of glaciers, and that of glaciers to regional scales, we estimate the spatial ranges at which errors are correlated. Where relevant, we perform this propagation by estimating the standard error



with a number of effective samples (N_{eff}) that accounts for spatial correlations. We derive the number of effective samples by numerically integrating a sum of variogram models fitted to our empirical variograms within a circular area of the same size as the glacier (Figure 4; Hugonnet et al., 2021). This is a generalisation of the approach by Rolstad et al. (2009). We use the implementation in *xdem* based on spatial statistics of the *scikit-gstat* Python package (Mälicke, 2021).

3.5.1 Mean elevation change uncertainty

Multiple intermediate steps in the photogrammetric pipeline can distort the DEMs and orthoimages. Those include image scanning artefacts, camera model uncertainties, image noise, image location and orientation error, as well as subsequent methodological shortcomings (Dehecq et al., 2020). We quantify the uncertainty comprising these errors by comparing terrain assumed to be stable in our elevation change estimates. The stable terrain excludes ice, perennial snow patches (Freudiger et al., 2018) and lakes. Dams created between the 1920s and 1980s are especially important to exclude, as they otherwise introduce unwanted positive changes of up to >50 m. While other factors such as landslides, vegetation change and buildings may also affect stable terrain, visual inspection showed no obvious signs for their presence.

For DEMs generated by satellite or airborne photogrammetry, elevation change errors often vary with terrain aspect, slope, or curvature (Toutin, 2002; Hugonnet et al., 2021). Here, we find no dependency of the elevation change uncertainty to these terrain attributes. We suspect that this is the result of the large number of DEMs that is used in our mosaic. Indeed, also DEMs derived from terrestrial images might be affected by such attribute-dependent errors, but since the individual DEM tiles are derived independently from independent set of images, these might cancel out when aggregated over several glaciers. We thus assume that our elevation uncertainty is stationary in space, and estimate it by using the Normalized Median Absolute Deviation (NMAD) of the elevation change estimates on stable terrain.

We account for spatial correlation of elevation change uncertainty by fitting a double spherical variogram model to the empirical variogram of elevation changes (Figure 4D+E), thereby modelling short- and long-range correlations (respectively in stable terrain residuals, panel E, and interpolation errors, panel D). We then estimate the uncertainty in the mean elevation change σ by circular integration of the sum of variogram models over the glacier area A (Rolstad et al., 2009; Hugonnet et al., 2021):

$$\sigma = \frac{2\pi}{A} \int_{r=0}^{\sqrt{A/\pi}} [\sigma_p - \gamma(r)] dr = \frac{\sigma_p}{\sqrt{N_{\text{eff}}}} \quad (6)$$

where σ_p is the NMAD of elevation differences on stable terrain, $\gamma(r)$ is the sum of variogram models with spatial lag r and N_{eff} is the number of effective samples.

3.5.2 Glacier outline uncertainty

We identify three major sources of uncertainties from the glacier outlines drawn from the LK50 maps: the georeferencing error of the map, the timing uncertainty of the used topographic data (which was assumed to largely be the TerrA dataset), and the



errors in manual delineation (including the subsequent digitisation from the map) of a glacier front. The temporal concurrency of the LK50 map to the Terra imagery particularly needs validation, as the degree at which data from other times was used is unknown. In the case where the outlines are spatially consistent with the Terra dataset, the concurrency assumption is verified.

275 We evaluate these three uncertainty sources combined by digitizing sparse outlines at 61 sites from orthorectified versions of the photographs generated in the photogrammetric pipeline. We then compare their general agreement with the LK50 glacier outlines. Outlines drawn from orthoimages will have a perfect relative georeferencing to the DEMs, and should thus only differ from the LK50 outlines due to the subjective nature of glacier delineation. For this comparison, we draw lines from the centroid of each glacier toward arbitrary points on the digitized outline and measure the distance to each LK50 and orthoimage-derived
280 outline intersection. We use the difference between the two as a metric of the variability in spatial extent (Figure 5B).

We find a resultant median length difference of 7.9 m; the LK50 outlines are generally less extensive, potentially due to manual delineation differences in including or excluding glacier-marginal snow cover, with an NMAD of 28.06 m. Finally, in order to propagate these delineation differences into a source of elevation changes uncertainties, we first dilate (i.e. enlarge) and erode (i.e. shrink) the mask by the systematic difference (7.9 m). We then estimate the glacier outline uncertainty by computing
285 the average difference between the initial mask and the dilated or eroded masks:

$$\sigma_{area} = \frac{\left| \overline{\left[\frac{dH}{dt} \right]_D} - \overline{\left[\frac{dH}{dt} \right]_E} \right|}{2}, \quad (7)$$

where $\overline{\left[\frac{dH}{dt} \right]_D}$ is the mean elevation change rate within the dilated mask, and $\overline{\left[\frac{dH}{dt} \right]_E}$ is the mean elevation change rate within the eroded mask.

3.5.3 Interpolation uncertainty

290 We estimate the uncertainty in the interpolation approach by artificially introducing gaps in the gap-free elevation changes of Hugonnet et al. (2021). These elevation changes are based on stereo-correlation of optical satellite imagery from the Advanced Spaceborne Thermal Emission and Reflection Radiometer (ASTER), which cover the entire study area, and refer to the period 2000–2020. We interpolate the introduced gaps using our approach, and study the difference between the interpolated ASTER elevation changes and the original ASTER elevation change estimates. We use this difference solely to compute the spatial
295 correlation of uncertainties. For this, we fit a double spherical variogram model to the empirical variogram of the above difference in elevation change. We thereby measure the spatial correlation range of the error of interpolated elevation changes (Figure 4D). In order to scale the variance of our interpolation uncertainty σ_{int} correctly, we did not use the NMAD of ASTER differences which have a different absolute magnitude, and might be polluted by a lesser vertical precision. Instead, we interpolate the Terra elevation changes in all pixels, and then use the NMAD of the difference between the original and
300 interpolated elevation change estimates.

We find strong correlations of interpolated elevation change errors at small scales, which fully decorrelate at a spatial lag of approximately 2,100 m. This indicates that errors are well correlated at the glacier-scale, but are largely independent among



glaciers of a given region. We thus propagate our interpolation uncertainties from pixel to glacier, and from glacier to region accordingly, and add a 0.01 m a^{-1} median bias that we observe from the interpolation step.

305 3.5.4 Temporal correction uncertainty

We perform our temporal correction using modelled mass balance estimates, whose uncertainties accumulate over time. The reported uncertainty for one year's specific mass balance (σ_B) is approximately $0.2 \text{ m w.e. a}^{-1}$ (Zemp et al., 2013). We derive the uncertainty in the temporal correction by standard propagation of independent uncertainties:

$$\sigma_{time}^2 = \left[\frac{dH}{dt} \right]^2 \times \left[\frac{2\sigma_B^2}{B(2016) - B(1931)} + \frac{2\sigma_B^2}{B(t_1) - B(t_0)} \right] \times \left(\frac{B(2016) - B(1931)}{B(t_1) - B(t_0)} \right)^2, \quad (8)$$

310 where $B(t)$ is the cumulative mass balance for year t , and where the correction is done for the time period t_0 – t_1 .

3.5.5 Total elevation change uncertainty

We calculate the total glacier-specific and regional uncertainty in mass balance by the squared sums of all error components, accounting for the number of effective samples (N_{eff}) derived from the variograms where appropriate:

$$\sigma_{total}^2 = \left(\frac{\sigma_{topo}}{\sqrt{N_{topo}}} \right)^2 + \sigma_{time}^2 + \sigma_{area}^2 + \left(\frac{\sigma_{int}}{\sqrt{N_{int}}} \right)^2 + \left(\frac{|\dot{B}| \times \sigma_{\rho\Delta V}}{\rho\Delta V} \right)^2 \quad (9)$$

315 Here, σ_{topo} is the NMAD of the stable terrain difference, N_{topo} is the number of effective samples calculated from the stable terrain variogram model (Figure 4E) and using Equation 6, σ_{int} is the NMAD of the difference between the artificially removed and interpolated pixels, N_{int} is the number of effective samples calculated from the interpolation error variogram model (Figure 4D, Equation 6), $|\dot{B}|$ is the absolute average mass balance rate for the glacier or region, and $\sigma_{\rho\Delta V} = 60 \text{ kg m}^{-3}$ is the uncertainty of the factor used for volume-to-mass conversions (Huss, 2013).

320 4 Results

For the period 1931–2016, our results indicate an average glacier volume loss of $-0.73 \pm 0.08 \text{ km}^3 \text{ a}^{-1}$, and a mean annual specific mass balance of $-0.52 \pm 0.09 \text{ m w.e. a}^{-1}$ (Table 2). With a total Swiss glacier volume of $58.7 \pm 2.5 \text{ km}^3$ in 2016 (Grab et al., 2021), this corresponds to a loss of $0.86 \pm 0.08\%$ per year in comparison to the 1931–2016 average volume. Integration of these changes over the considered period provides a total glacier volume loss of $51 \pm 6\%$ since 1931. The total glacier area
 325 concomitantly reduced by $5.9 \pm 0.8 \text{ km}^2 \text{ a}^{-1}$, corresponding to an area loss of 35.7% (the total glacier area was of $1494 \pm 69 \text{ km}^2$ in ca. 1931, and of $961 \pm 22 \text{ km}^2$ in 2016).

We analyse the spatial variability in mass balance over a regular grid of $30 \text{ km} \times 30 \text{ km}$ (Figure 7). The results show relatively high spatial variability, as shown by the ca. $1.5 \times$ larger mass loss rates in the Aletsch region compared to the Southern Valais



Alps. On the same grid, we observe a minimum regional loss of $0.32 \text{ m w.e. a}^{-1}$ in the south west, and a maximum loss of
330 $1.02 \text{ m w.e. a}^{-1}$ in the north east (only cells with more than five glaciers are considered).

Analysing the regional mass balance as a function of easting and river basin (Figure 8) reveals a clustered elevation dependency for individual basins. In general, glaciers in the central part of the Rhone basin have a higher elevation range and lower mass loss compared to other basins. We also observe a Pearson correlation coefficient of $r = 0.42$ between glacier mass balance and median elevation (Figure 9A), indicating that lower glaciers appear to experience higher mass loss rates. We deem this
335 correlation to be significant (Gignac and Szodorai, 2016). From these two results, we can conclude that the spatial variability is largely influenced by glaciers' elevation range.

Weaker correlations with other morpho-topographic characteristics are detected as well. For example, we observe a correlation between glacier mass balance and the mean slope of the lowest 10th percentile of elevation ($r = 0.28$; "terminus slope"; Figure 9C), and a similar negative relationship with modern fractional debris cover ($r = -0.28$; Figure 9D). This indicates
340 that glaciers with flatter termini or higher debris cover tend to experience higher mass loss rates as their steeper and ice-free counterparts. These findings support the results from studies performed with smaller subsets of glaciers (Huss, 2012), over shorter time spans (Fischer et al., 2015), in different geographical regions (Brun et al., 2019; Geyman et al., 2022), and based on area-change data (Linsbauer et al., 2021).

5 Discussion

345 5.1 Comparison with map data

The current consensus on the magnitude of Swiss glacier changes over the 20th century stems from (i) the work by Bauder et al. (2007), who derived glacier volume changes from the digitization of topographic maps for about 40 large glaciers, as well as the evaluation of repeated aerial photogrammetrical surveys after 1960; and (ii) the combination of these datasets with direct glaciological measurements and modelling presented by Huss et al. (2010a, c); GLAMOS (1881–2020). From the dataset
350 by Bauder et al. (2007), we extract the average annual mass balance for each of the 39 glaciers with data, homogenized to the study period 1931–2016 with annual data from Huss et al. (2010a). The overall uncertainty in this glacier-specific mass balance dataset is determined by the accuracy of the DEMs used for constraining long-term mass change and only marginally the modelling providing annual variations. By using an approach similar as outlined in Sec. 3.5, we recompute the centennial uncertainty in the data by Bauder et al. (2007) and Huss et al. (2010a) allowing for conservative estimates of components that
355 are difficult to be inferred retrospectively. We find that for most individual glaciers, uncertainties are around $0.2 \text{ m w.e. a}^{-1}$ when considering the entire period of interest. The comparison to results of the present study at the scale of the individual glaciers generally shows a good agreement ($r=0.71$, Figure 10A), although the independent glacier-specific dataset (Bauder et al., 2007; Huss et al., 2010a) indicates a mass loss rate that is, on average, $0.08 \text{ m w.e. a}^{-1}$ smaller than in our study.

For Grosser Aletschgletscher (location shown in Figure 6), we additionally compare the map data digitized by Bauder et al.
360 (2007) to the DEM mosaic we generated for 1926 and 1927. The mean thickness change derived from the map is -56 m (with an unknown uncertainty) between 1927 and 2017 (Figure 10B) while the results of our study suggest a change of $-72 \pm 10 \text{ m}$



(Figure 10C). Comparing the two DEMs, an elevation dependent difference is seen (Figure 10D+E): they generally agree in the accumulation area, but deviate considerably at the glacier tongue. We attribute this difference to either (i) poor georeferencing of either datasets, (ii) temporal inconsistencies in the map data, which might not represent the year 1927 uniformly, or (iii) a combination of these factors. Also note that for being consistent with Bauder et al. (2007), the above values are obtained by excluding the tributary Mittelaletschgletscher. Before 1969, the latter was confluent with Grosser Aletschgletscher (GLAMOS, 1881–2020), which is also reflected in the LK50 outlines, and its omission might contribute in explaining differences at other localities between the two studies.

The above comparison also reveals a potential shortcoming of our interpolation approach near the glacier margins. Indeed, the proximity to glacier margins was not considered, meaning that changes can be overestimated at these specific locations. The problem arises from the fact that our gap-filling procedure is based on the multiplication of the average ice-thickness change rate observed at a given elevation with the length of the considered time period (i.e. 1931-2016, on average). This results in a total, elevation-dependent ice thickness change that is added back to the SwissALTI3D DEM. For a given location, however, the actual surface elevation in 1931 might have been smaller, especially if the location has become ice free before 2016. The latter case is most often encountered near the glacier margins, thus explaining the pattern of differences observed in Figures 10D and 10E.

Whilst the shortcoming is inherently accounted for in our uncertainty analysis, we suggest that future studies could improve the interpolation technique used here. Auxiliary information on the timing at which a given location has become ice free might help with that. Assuming that the uncertainty of the maps used by Bauder et al. (2007) is similar or larger than in our study, however, the 95% confidence intervals of the mean thickness change overlap. In summary, this means that the two studies agree within their respective uncertainties.

5.2 Advantages and challenges of digital reanalysis

Reanalysis of the source material is a clear step forward compared to a map-based analysis. This is because the creation of topographic maps requires considerable interpretation, and sometimes qualified guesswork to connect points of known elevation with continuous contour lines. The two factors make for a vague border between actual data and subjective inter- or extrapolations. Comparisons between glacier extents obtained from digitized maps and modern digital photogrammetric reconstructions show significantly reduced biases for the latter (e.g. Koblet et al., 2010; Midgley and Tonkin, 2017; Geyman et al., 2022). In addition, many maps are temporally inconsistent, because maps are asynchronously updated with newer data that are added to older maps during successive revisions. Problematic in this respect is the fact that, at least for Switzerland, the exact year of the data sources used during such revisions is mostly unknown (Fischer et al., 2015). For the second half of the 20th century, however, clearly dated and complete surveys based on aerial photogrammetry are available for glaciers with long-term monitoring programmes (Bauder et al., 2007), thus circumventing this problem for the more recent decades.

While the temporal consistency of our results is warranted in general, some uncertainty is introduced through the temporal correction required for individual glaciers (between 0.00 and 0.09 m w.e. a^{-1} for individual glaciers; see Sec. 3.3.1; Figure 4B). The temporal inhomogeneity of country-wide results is inherent to any analysis that is based on terrestrial surveys. Indeed, the



sheer time required to acquire such data will always lead to a temporal spread in the acquisition times. Whilst this problem is decreasing in importance for modern surveys thanks to a wider image swath, the analysis on historic photographs requires careful consideration of the issue. We suggest that temporal corrections in line with (or better than) our study are a fundamental step in post-processing and interpreting the results derived from historic terrestrial surveys.

400 Future improvements of our workflow may help further increasing the spatial coverage of the dataset and reducing co-
registration errors. The interpolation necessary over 55% of the analysed area was the largest contributor of uncertainty in our
analysis (0.00–0.39 m w.e. a^{-1} for individual glaciers; Figure 4B). Higher coverage, or a more accurate interpolation method-
ology, may lower this. The Terra dataset has a theoretical maximum glacier coverage of ca. 86%, meaning that only about half
of the theoretical maximum coverage was realised in our reconstruction. Newer photogrammetric methods, especially those
405 rooted in the machine learning domain (e.g. Mildenhall et al., 2020; Zheng et al., 2020), can help improving feature description
or depth reconstruction. These may therefore pave the way to an increased coverage when compared to the methods currently
implemented in Agisoft Metashape. In this respect, we attempted to replace the feature matcher with ASIFT (Morel and Yu,
2009), but long processing times and a general lack of robustness to image noise led us abandon the idea. The uncertainty
analyses of this study show that the regional aggregates are accurate, thus indicating that a reanalysis of the Terra imagery
410 with modern methods may be worthwhile especially if interested in individual glaciers.

It is remarkable that reanalyses such as presented here, or as alluded to above, are possible at all for a dataset that is almost
hundred years old, and in some cases even older. This possibility is only provided by the systematic, thorough, and meticulous
archiving that was performed at that time, and by the preservation-efforts that were invested since then. The Swiss Federal
Office of Topography deserves credit for this. In this context, it is interesting to note that what have now become known as
415 the “FAIR Guiding Principles for scientific data” (Wilkinson et al., 2016) were respected over the course of almost a century.
Indeed, the FAIR principles require the data to be findable (F), accessible (A), interoperable (I), and reusable (R), and all
of these criteria are met for the terra archive: the images are easily found and accessed via swisstopo’s geodata portal¹, are
made interoperable by being distributed in a commonly accepted digital data format, and are reusable thanks to the rich and
self-explaining metadata that complement the individual images. Similar database exist in many other countries including, and
420 not limited to, the United States of America², France³ and Sweden⁴. We encourage data holders and archivists alike to follow
such examples, and hope that our study can be an example demonstrating the added value of such long-term archiving efforts.

6 Conclusions

In this study, we utilise 21,703 terrestrial photographs from the “Terra” archive recently made accessible by the Swiss Federal
Office of Topography to quantify glacier change over the entire Swiss Alps since 1931. We take advantage of modern pho-
425 togrammetric techniques and the software Agisoft Metashape to reprocess the scanned images in a semi-automated fashion. We

¹<https://www.swisstopo.admin.ch/en/geodata/images/terrestrial.html> (last accessed 19/01/2022)

²<https://earthexplorer.usgs.gov> (last accessed 19/01/2022)

³<https://remonterletemps.ign.fr> (last accessed 19/01/2022)

⁴<https://www.alvin-portal.org>, (last accessed 19/01/2022)



use the procedure to reconstruct the ca. 1931 topography for 45% of the glaciers in the region. We estimate a Swiss-wide glacier mass balance of -0.52 ± 0.09 m w.e. a^{-1} and an area reduction of 5.9 ± 0.8 km² a^{-1} between 1931 and 2016. This translates to a halving of glacier volume compared to 2016, and a third's reduction in areal cover. Our results indicate a strong spatial variability in glacier thinning, with glaciers in the north east losing mass twice as rapidly as in the south west of Switzerland.
430 This variability is partially explained by the fact that mass losses are found to be pronounced for glaciers at a lower elevation, with more gently-sloping termini, and with a high present-day debris-cover fraction.

While our approach which relies on the full breadth of original image data from almost one century ago was successful in obtaining regional estimates, observations at the local scale are still uncertain for the analysis of individual glaciers. Uncertainties in our estimates are particularly dominated by a fragmented spatial coverage and the temporal heterogeneity of the Terra
435 acquisitions, which account for 33% and 32% of the uncertainties, respectively. Among the main challenges of dealing with such terrestrial archives are (1) the limited extent of the observed area, hence reducing the amount of stable terrain available for DEM co-registration, (2) the low incidence angle of the images that causes geometric distortions, and (3) the long time span between acquisitions. While all these issues are inherent to terrestrial images, the first two challenges call for improved image processing methods to find correspondences between images acquired with strongly differing view-angles if improved
440 small-scale accuracy is sought. The combination of remote sensing, in situ observations and modelling was the key in solving the third challenge and providing a temporally consistent estimate.

Ultimately, our results validate numbers that were only previously inferred by extrapolation from sparse data. In a period of rapid air temperature increase, regional mass balance data over a time span of almost one century are essential to accurately understand how glaciers respond to changes in climate. The reconstructions of this study, among other recently published
445 datasets of regional scope, may mark a milestone for further understanding of past, current and future glacier change. The approaches developed here are expected to offer a high potential for evaluating historical datasets with modern technology.

Acknowledgements. We would like to thank swisstopo for acquiring, archiving, scanning and distributing the Terra images. This work would not have been possible without over a hundred years of efforts. We are particularly grateful to Philip Joerg and Matthias Zesiger for providing additional details on the images metadata and acquisition. We are grateful to Roxana Zehtabchi for early developments of the data processing
450 workflow. We would like to thank Timothée Produit and Adrien Gressin (HEIG-Vaud) for sharing initial Terra viewsheds and for discussions on the Terra archive. This project was funded by the Federal Office of Meteorology and Climatology MeteoSwiss in the framework of GCOS Switzerland.

Code and data availability. The source code of the photogrammetric analysis is available at: <https://github.com/VAW-SwissTerra/SwissTerra>. The code for post-processing, uncertainty, and mass balance is available at: <https://github.com/VAW-SwissTerra/terradem>.

455 A link to all data will be added here before final publication of this manuscript.



Author contributions. AD and DF conceived the study. EM wrote the study code and performed the analyses with main input from AD, as well as RH and DF. EM made the figures and wrote the majority of the manuscript with inputs from AD, RH, MH, EH and DF. EM and EH created the LK50 glacier outline inventory. AD and RH contributed with *xdem* code and analyses. EH, MH and AB contributed with data to the analysis. All authors contributed to the manuscript text.

460 *Competing interests.* The authors report no competing interests.



References

- Bauder, A., Funk, M., and Huss, M.: Ice-volume changes of selected glaciers in the Swiss Alps since the end of the 19th century, *Annals of Glaciology*, 46, 145–149, <https://doi.org/10.3189/172756407782871701>, 2007.
- 465 Belart, J. M. C., Magnússon, E., Berthier, E., Gunnlaugsson, A. T., Pálsson, F., Aðalgeirsdóttir, G., Jóhannesson, T., Thorsteinsson, T., and Björnsson, H.: Mass Balance of 14 Icelandic Glaciers, 1945–2017: Spatial Variations and Links With Climate, *Frontiers in Earth Science*, 8, 163, <https://doi.org/10.3389/feart.2020.00163>, 2020.
- Beniston, M., Farinotti, D., Stoffel, M., Andreassen, L. M., Coppola, E., Eckert, N., Fantini, A., Giacona, F., Hauck, C., Huss, M., Huwald, H., Lehning, M., López-Moreno, J.-I., Magnusson, J., Marty, C., Morán-Tejeda, E., Morin, S., Naaim, M., Provenzale, A., Rabatel, A., Six, D., Stötter, J., Strasser, U., Terzago, S., and Vincent, C.: The European mountain cryosphere: a review of its current state, trends, and
470 future challenges, *The Cryosphere*, 12, 759–794, <https://doi.org/10.5194/tc-12-759-2018>, 2018.
- Brun, F., Wagnon, P., Berthier, E., Jomelli, V., Maharjan, S. B., Shrestha, F., and Kraaijenbrink, P. D. A.: Heterogeneous Influence of Glacier Morphology on the Mass Balance Variability in High Mountain Asia, *Journal of Geophysical Research: Earth Surface*, 124, 1331–1345, <https://doi.org/10.1029/2018JF004838>, 2019.
- Cox, L. H. and March, R. S.: Comparison of geodetic and glaciological mass-balance techniques, Gulkana Glacier, Alaska, U.S.A., *Journal of Glaciology*, 50, 363–370, <https://doi.org/10.3189/172756504781829855>, 2004.
475
- Dehecq, A., Gardner, A. S., Alexandrov, O., McMichael, S., Hugonnet, R., Shean, D., and Marty, M.: Automated Processing of De-classified KH-9 Hexagon Satellite Images for Global Elevation Change Analysis Since the 1970s, *Frontiers in Earth Science*, 8, 516, <https://doi.org/10.3389/feart.2020.566802>, 2020.
- Fischer, M., Huss, M., and Hoelzle, M.: Surface elevation and mass changes of all Swiss glaciers 1980–2010, *The Cryosphere*, 9, 525–540,
480 <https://doi.org/10.5194/tc-9-525-2015>, 2015.
- Freudiger, D., Mennekes, D., Seibert, J., and Weiler, M.: Historical glacier outlines from digitized topographic maps of the Swiss Alps, *Earth System Science Data*, 10, 805–814, <https://doi.org/10.5194/essd-10-805-2018>, 2018.
- Geyman, E. C., van Pelt, W. J. J., Maloof, A. C., Faste Aas, H., and Kohler, J.: Historical glacier change on Svalbard predicts doubling of mass loss by 2100, *Nature*, 601, 374–395, <https://doi.org/10.1038/s41586-021-04314-4>, 2022.
- 485 Gignac, G. E. and Szodorai, E. T.: Effect size guidelines for individual differences researchers, *Personality and Individual Differences*, 102, 74–78, <https://doi.org/https://doi.org/10.1016/j.paid.2016.06.069>, 2016.
- Girod, L., Nielsen, N. I., Couderette, F., Nuth, C., and Käab, A.: Precise DEM extraction from Svalbard using 1936 high oblique imagery, *Geoscientific Instrumentation, Methods and Data Systems*, 7, 277–288, <https://doi.org/10.5194/gi-7-277-2018>, 2018.
- GLAMOS: The Swiss Glaciers 1880-2018/19, *Glaciological Reports No 1-140*, Yearbooks of the Cryospheric Commission of the Swiss
490 Academy of Sciences (SCNAT), published since 1964 by VAW / ETH Zurich, https://doi.org/10.18752/glrep_series, 1881–2020.
- GLAMOS: The Swiss Glaciers 2015/16 and 2016/17: *Glaciological Report No. 137/138*, *Glaciological Report No. 137/138* of the Cryospheric Commission (EKK) of the Swiss Academy of Sciences (SCNAT) published by VAW / ETH Zürich, https://doi.org/10.18752/glrep_137-138, 2018.
- GLAMOS: Swiss Glacier Mass Balance 2020 (release 2021), <https://doi.org/10.18750/MASSBALANCE.2020.R2021>, type: dataset, 2021.
- 495 Grab, M., Mattea, E., Bauder, A., Huss, M., Rabenstein, L., Hodel, E., Linsbauer, A., Langhammer, L., Schmid, L., Church, G., Hellmann, S., Délèze, K., Schaer, P., Lathion, P., Farinotti, D., and Maurer, H.: Ice thickness distribution of all Swiss glaciers based on extended ground-penetrating radar data and glaciological modeling, *Journal of Glaciology*, pp. 1–19, <https://doi.org/10.1017/jog.2021.55>, 2021.



- Holmlund, E. S.: Aldegondabreen glacier change since 1910 from structure-from-motion photogrammetry of archived terrestrial and aerial photographs: utility of a historic archive to obtain century-scale Svalbard glacier mass losses, *Journal of Glaciology*, 67, 107–116, <https://doi.org/10.1017/jog.2020.89>, publisher: Cambridge University Press, 2021.
- Holmlund, E. S. and Holmlund, P.: Constraining 135 Years of Mass Balance with Historic Structure-from-Motion Photogrammetry on Storglaciären, Sweden, *Geografiska Annaler: Series A, Physical Geography*, <https://doi.org/10.1080/04353676.2019.1588543>, 2019.
- Hugonnet, R., McNabb, R., Berthier, E., Menounos, B., Nuth, C., Girod, L., Farinotti, D., Huss, M., Dussaillant, I., Brun, F., and Kääh, A.: Accelerated global glacier mass loss in the early twenty-first century, *Nature*, 592, 726–731, <https://doi.org/10.1038/s41586-021-03436-z>, 2021.
- Huss, M.: Extrapolating glacier mass balance to the mountain-range scale: the European Alps 1900–2100, *The Cryosphere*, 6, 713–727, <https://doi.org/10.5194/tc-6-713-2012>, 2012.
- Huss, M.: Density assumptions for converting geodetic glacier volume change to mass change, *The Cryosphere*, 7, 877–887, <https://doi.org/10.5194/tc-7-877-2013>, 2013.
- Huss, M., Bauder, A., Funk, M., and Hock, R.: Determination of the seasonal mass balance of four Alpine glaciers since 1865, *Journal of Geophysical Research*, 113, F01 015, <https://doi.org/10.1029/2007JF000803>, 2008.
- Huss, M., Hock, R., Bauder, A., and Funk, M.: 100-year mass changes in the Swiss Alps linked to the Atlantic Multi-decadal Oscillation: THE 100-YEAR MASS CHANGE OF ALPINE GLACIERS, *Geophysical Research Letters*, 37, n/a–n/a, <https://doi.org/10.1029/2010GL042616>, 2010a.
- Huss, M., Juvet, G., Farinotti, D., and Bauder, A.: Future high-mountain hydrology: a new parameterization of glacier retreat, *Hydrology and Earth System Sciences*, 14, 815–829, <https://doi.org/10.5194/hess-14-815-2010>, 2010b.
- Huss, M., Usselman, S., Farinotti, D., and Bauder, A.: Glacier mass balance in the south-eastern Swiss Alps since 1900 and perspectives for the future, *ERDKUNDE*, 2010, 119–140, <https://doi.org/10.3112/erdkunde.2010.02.02>, 2010c.
- Huss, M., Dhulst, L., and Bauder, A.: New long-term mass-balance series for the Swiss Alps, *Journal of Glaciology*, 61, 551–562, <https://doi.org/10.3189/2015JoG15J015>, 2015.
- Huss, M., Bauder, A., Linsbauer, A., Gabbi, J., Kappenberger, G., Steinegger, U., and Farinotti, D.: More than a century of direct glacier mass-balance observations on Claridenfirn, Switzerland, *Journal of Glaciology*, 67, 697–713, <https://doi.org/10.1017/jog.2021.22>, 2021.
- Koblet, T., Gärtner-Roer, I., Zemp, M., Jansson, P., Thee, P., Haeblerli, W., and Holmlund, P.: Reanalysis of multi-temporal aerial images of Storglaciären, Sweden (1959-99) Part 1: Determination of length, area, and volume changes, *The Cryosphere*, 4, 333–343, <https://doi.org/10.5194/tc-4-333-2010>, 2010.
- Linsbauer, A., Huss, M., Hodel, E., Bauder, A., Fischer, M., Weidmann, Y., Bärtschi, H., and Schmassmann, E.: The New Swiss Glacier Inventory SGI2016: From a Topographical to a Glaciological Dataset, *Frontiers in Earth Science*, 9, 774, <https://doi.org/10.3389/feart.2021.704189>, 2021.
- Maurer, J. M., Schaefer, J. M., Rupper, S., and Corley, A.: Acceleration of ice loss across the Himalayas over the past 40 years, *Science Advances*, 5, eaav7266, <https://doi.org/10.1126/sciadv.aav7266>, 2019.
- McNabb, R., Nuth, C., Kääh, A., and Girod, L.: Sensitivity of glacier volume change estimation to DEM void interpolation, *The Cryosphere*, 13, 895–910, <https://doi.org/10.5194/tc-13-895-2019>, 2019.
- Mertes, J. R., Gulley, J. D., Benn, D. I., Thompson, S. S., and Nicholson, L. I.: Using structure-from-motion to create glacier DEMs and orthoimagery from historical terrestrial and oblique aerial imagery: SfM on Differing Historical Glacier Imagery Sets, *Earth Surface Processes and Landforms*, 42, 2350–2364, <https://doi.org/10.1002/esp.4188>, 2017.



- MeteoSwiss: Homogeneous data series since 1864, <https://www.meteoswiss.admin.ch/home/climate/swiss-climate-in-detail/homogeneous-data-series-since-1864.html>, 2021.
- Midgley, N. and Tonkin, T.: Reconstruction of former glacier surface topography from archive oblique aerial images, *Geomorphology*, 282, 18–26, <https://doi.org/10.1016/j.geomorph.2017.01.008>, 2017.
- 540 Mildenhall, B., Srinivasan, P. P., Tancik, M., Barron, J. T., Ramamoorthi, R., and Ng, R.: NeRF: Representing Scenes as Neural Radiance Fields for View Synthesis, in: *Computer Vision – ECCV 2020*, vol. 12346, pp. 405–421, Springer International Publishing, Cham, https://doi.org/10.1007/978-3-030-58452-8_24, 2020.
- Morel, J.-M. and Yu, G.: ASIFT: A New Framework for Fully Affine Invariant Image Comparison, *SIAM Journal on Imaging Sciences*, 2, 438–469, <https://doi.org/10.1137/080732730>, 2009.
- 545 Müller, F., Caffisch, A., and Müller, G.: *Firn und Eis der Schweizer Alpen: Gletscherinventar*, Publ. / Geographisches Institut, Eidgenössische Technische Hochschule, 57-57a, 1976.
- Mälicke, M.: SciKit-GStat 1.0: A SciPy flavoured geostatistical variogram estimation toolbox written in Python, *Geoscientific Model Development Discussions*, pp. 1–43, <https://doi.org/10.5194/gmd-2021-174>, 2021.
- OpenCV contributors: Open Source Computer Vision Library, <https://opencv.org/>, 2021.
- 550 RGI: Randolph Glacier Inventory 6.0, <https://doi.org/10.7265/N5-RGI-60>, type: dataset, 2017.
- Rickenbacher, M.: *Konzeptbericht zu den terrestrischen Aufnahmen (TerrA)*, Tech. rep., swisstopo, Wabern, Switzerland, 2012.
- Rolstad, C., Haug, T., and Denby, B.: Spatially integrated geodetic glacier mass balance and its uncertainty based on geostatistical analysis: application to the western Svartisen ice cap, Norway, *Journal of Glaciology*, 55, 666–680, <https://doi.org/10.3189/002214309789470950>, 2009.
- 555 Ryf, S. and Klöti, T.: *Massnahmenplan zur Erhaltung des raumrelevanten Kulturguts von swisstopo*, Tech. rep., swisstopo, Wabern, Switzerland, <https://www.swisstopo.admin.ch/de/wissen-fakten/geschichte-sammlungen/historische-bilder/massnahmenplan.html>, 2008.
- Shean, D. E., Bhushan, S., Montesano, P., Rounce, D. R., Arendt, A., and Osmanoglu, B.: A Systematic, Regional Assessment of High Mountain Asia Glacier Mass Balance, *Frontiers in Earth Science*, 7, 363, <https://doi.org/10.3389/feart.2019.00363>, 2020.
- swisstopo: *Historische Bilder der Schweizer Alpen*, https://www.swisstopo.admin.ch/de/home/meta/medieninformationen.detail.news.html/swisstopo-internet/news2018/news_release/20180531.html, 2018.
- 560 swisstopo: *swissALTI3D - The high precision digital elevation model of Switzerland*, 2019.
- swisstopo: *swissTLM3D - The large-scale topographic landscape model of Switzerland, Version 1.8.*, 2020.
- Thibert, E., Blanc, R., Vincent, C., and Eckert, N.: Glaciological and volumetric mass-balance measurements: error analysis over 51 years for Glacier de Sarennes, French Alps, *Journal of Glaciology*, 54, 522–532, <https://doi.org/10.3189/002214308785837093>, 2008.
- 565 Toutin, T.: Three-dimensional topographic mapping with ASTER stereo data in rugged topography, *IEEE Transactions on Geoscience and Remote Sensing*, 40, 2241–2247, <https://doi.org/10.1109/TGRS.2002.802878>, 2002.
- Vincent, C., Soruco, A., Six, D., and Le Meur, E.: Glacier thickening and decay analysis from 50 years of glaciological observations performed on Glacier d’Argentière, Mont Blanc area, France, *Annals of Glaciology*, 50, 73–79, <https://doi.org/10.3189/172756409787769500>, 2009.
- 570 Wilkinson, M. D., Dumontier, M., Aalbersberg, I. J., Appleton, G., Axton, M., Baak, A., Blomberg, N., Boiten, J.-W., da Silva Santos, L. B., Bourne, P. E., Bouwman, J., Brookes, A. J., Clark, T., Crosas, M., Dillo, I., Dumon, O., Edmunds, S., Evelo, C. T., Finkers, R., Gonzalez-Beltran, A., Gray, A. J. G., Groth, P., Goble, C., Grethe, J. S., Heringa, J., ’t Hoen, P. A. C., Hoof, R., Kuhn, T., Kok, R., Kok, J., Lusher, S. J., Martone, M. E., Mons, A., Packer, A. L., Persson, B., Rocca-Serra, P., Roos, M., van Schaik, R., Sansone, S.-A., Schultes,



- 575 E., Sengstag, T., Slater, T., Strawn, G., Swertz, M. A., Thompson, M., van der Lei, J., van Mulligen, E., Velterop, J., Waagmeester, A.,
Wittenburg, P., Wolstencroft, K., Zhao, J., and Mons, B.: The FAIR Guiding Principles for scientific data management and stewardship,
Scientific Data, 3, 160 018, <https://doi.org/10.1038/sdata.2016.18>, 2016.
- xdem contributors: xdem, <https://doi.org/10.5281/ZENODO.4809697>, language: en, 2021.
- Zemp, M., Jansson, P., Holmlund, P., Gärtner-Roer, I., Koblet, T., Thee, P., and Haerberli, W.: Reanalysis of multi-temporal aerial images
of Storglaciären, Sweden (1959-99) Part 2: Comparison of glaciological and volumetric mass balances, The Cryosphere, 4, 345–357,
580 <https://doi.org/10.5194/tc-4-345-2010>, 2010.
- Zemp, M., Thibert, E., Huss, M., Stumm, D., Rolstad Denby, C., Nuth, C., Nussbaumer, S. U., Moholdt, G., Mercer, A., Mayer, C., Joerg,
P. C., Jansson, P., Hynek, B., Fischer, A., Escher-Vetter, H., Elvehøy, H., and Andreassen, L. M.: Reanalysing glacier mass balance
measurement series, The Cryosphere, 7, 1227–1245, <https://doi.org/10.5194/tc-7-1227-2013>, 2013.
- Zemp, M., Huss, M., Thibert, E., Eckert, N., McNabb, R., Huber, J., Barandun, M., Machguth, H., Nussbaumer, S. U., Gärtner-Roer, I.,
585 Thomson, L., Paul, F., Maussion, F., Kutuzov, S., and Cogley, J. G.: Global glacier mass changes and their contributions to sea-level rise
from 1961 to 2016, Nature, 568, 382–386, <https://doi.org/10.1038/s41586-019-1071-0>, 2019.
- Zheng, Q., Shi, B., and Pan, G.: Summary study of data-driven photometric stereo methods, Virtual Reality & Intelligent Hardware, 2,
213–221, <https://doi.org/10.1016/j.vrih.2020.03.001>, 2020.



Table 1. Photogrammetric processing parameters. The “High” alignment quality and “Ultra High” dense cloud quality means using the full image resolution for each respective step. “Mild” (1/3 strength) dense cloud filtering is a proprietary Metashape filtering setting. Rows with “*” represent averages for each individual stereo-panorama.

<u>Fiducial matching</u>	
Manually identified fiducials	3,395
Automatically identified fiducials	19,123 (81%)
Automatic vs. manual RMSE	8.61 px (0.18 mm)
<u>Position correction</u>	
Initial position offset	2.66±5.91 m
Corrected position offset	0.70±5.18 m
<u>Agisoft Metashape</u>	
Mean subset (chunk) size	192 images (12 stereo-panoramas).
“Zeiss” camera focal lengths	194/195 mm
“Wild” camera focal lengths	150–240 mm
Alignment parameters	High quality, 4,000 tie points, 40,000 key points.
Mean tie point count*	6937
Mean tie point reprojection RMSE	0.94 px
Reference accuracies	±2 m in position / ±1° in rotation.
Dense cloud parameters	Ultra High quality, Mild filtering.
Mean dense cloud point count*	23,196,538
Gridding resolution	5 m×5 m.
Mean points per DEM pixel	299
<u>Post-processing</u>	
Mean stable terrain NMAD before/after co-registration*	0.32 m a ⁻¹ / 0.13 m a ⁻¹
Generated DEMs	1,907 out of 2,364 stereo-panoramas (81%).



Table 2. Swiss-wide change rates and total changes in specific mass balance (B), thickness, area, volume and mass from 1931–2016. See equations 2–5 for how these are calculated. The uncertainties are the 95% confidence intervals.

Parameter	Magnitude \pm uncertainty
Total ca. 1931 area (km ²)	1492 \pm 68
Total ca. 1931 volume (km ³)	121.1 \pm 6.7
Mass balance rate (m w.e. a ⁻¹)	-0.52 \pm 0.09
Area change rate (km ² a ⁻¹)	-6.1 \pm 0.8
Volume change rate (km ³ a ⁻¹)	-0.73 \pm 0.08
Mass change rate (Gt a ⁻¹)	-0.62 \pm 0.14
Total mass balance (m w.e.)	-43.8 \pm 8.0
Total area change (km ²)	-518 \pm 69
Total volume change (km ³)	-62.4 \pm 6.9
Total mass change (Gt)	-53 \pm 12

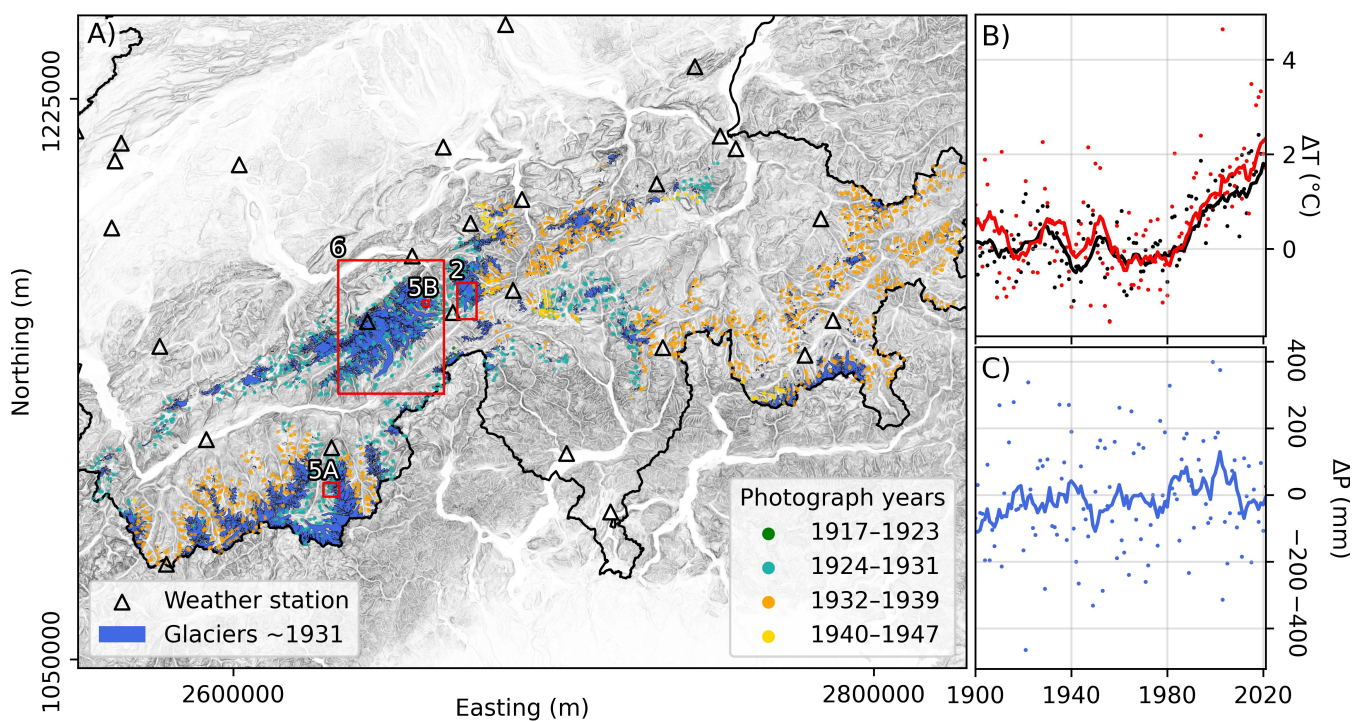


Figure 1. A) The distribution of Swiss glaciers around 1931 (blue areas). Country borders are outlined in black. The locations of the Terra photographs used in the study are shown with coloured dots, whose colour indicates the year of acquisition. The red boxes show the bounds of other figures (figure numbers given in white). B+C) Anomalies of mean annual (black) and mean summer (red) air temperature (B) and total precipitation (C) from 1961–1990. Ten year running averages are drawn as lines. The data are from 14 homogenized stations (triangles in A, MeteoSwiss, 2021).

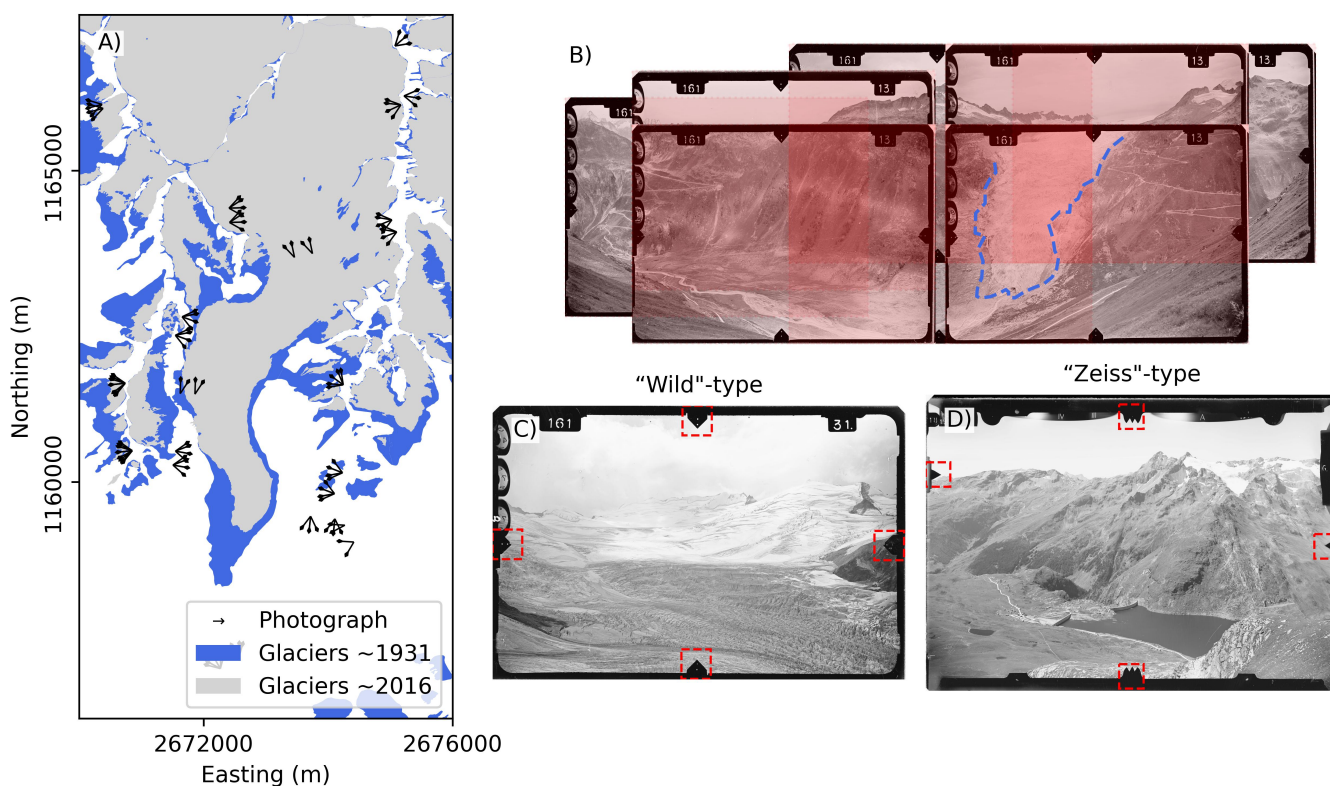


Figure 2. A) Imaging locations (black arrows pointing in the imaging direction) together with ca. 1931 (blue) and ~2016 (grey) glacier outlines for Rhonegletscher. B) Panorama example overlooking Rhonegletscher (outlined in dashed blue). The opaque red boxes show the coverage of each image. The darkest red indicates five images overlapping. C+D) Examples of a “Wild”- (C) and a “Zeiss”-type (D) photograph, and associated fiducial marks (framed in red).

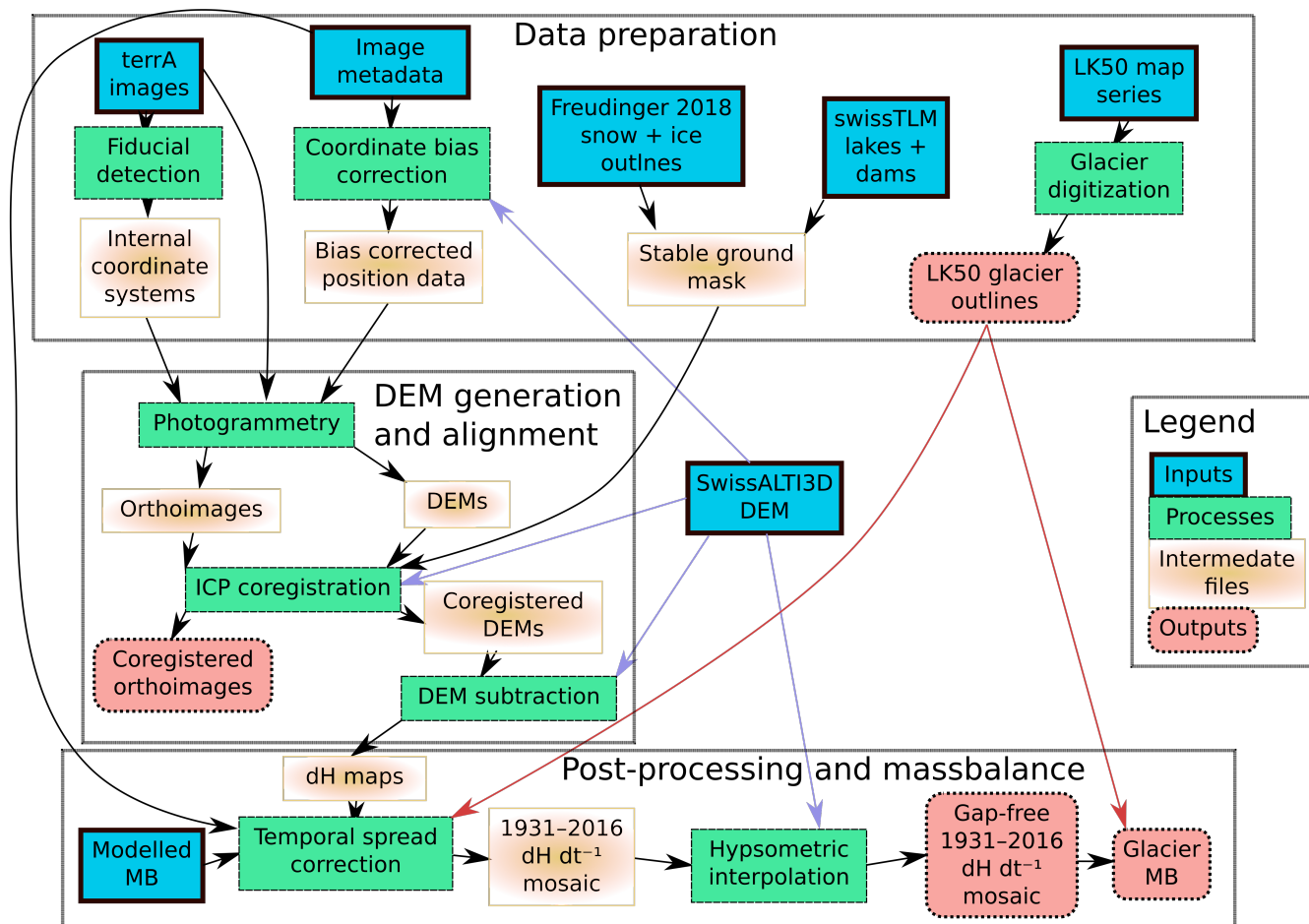


Figure 3. Flowchart synthesising the data processing. Inputs refer to the external data that were used, processes are different steps in the processing chain, and outputs are files of particular interest for this and future studies. All intermediate and output files are available for further use.

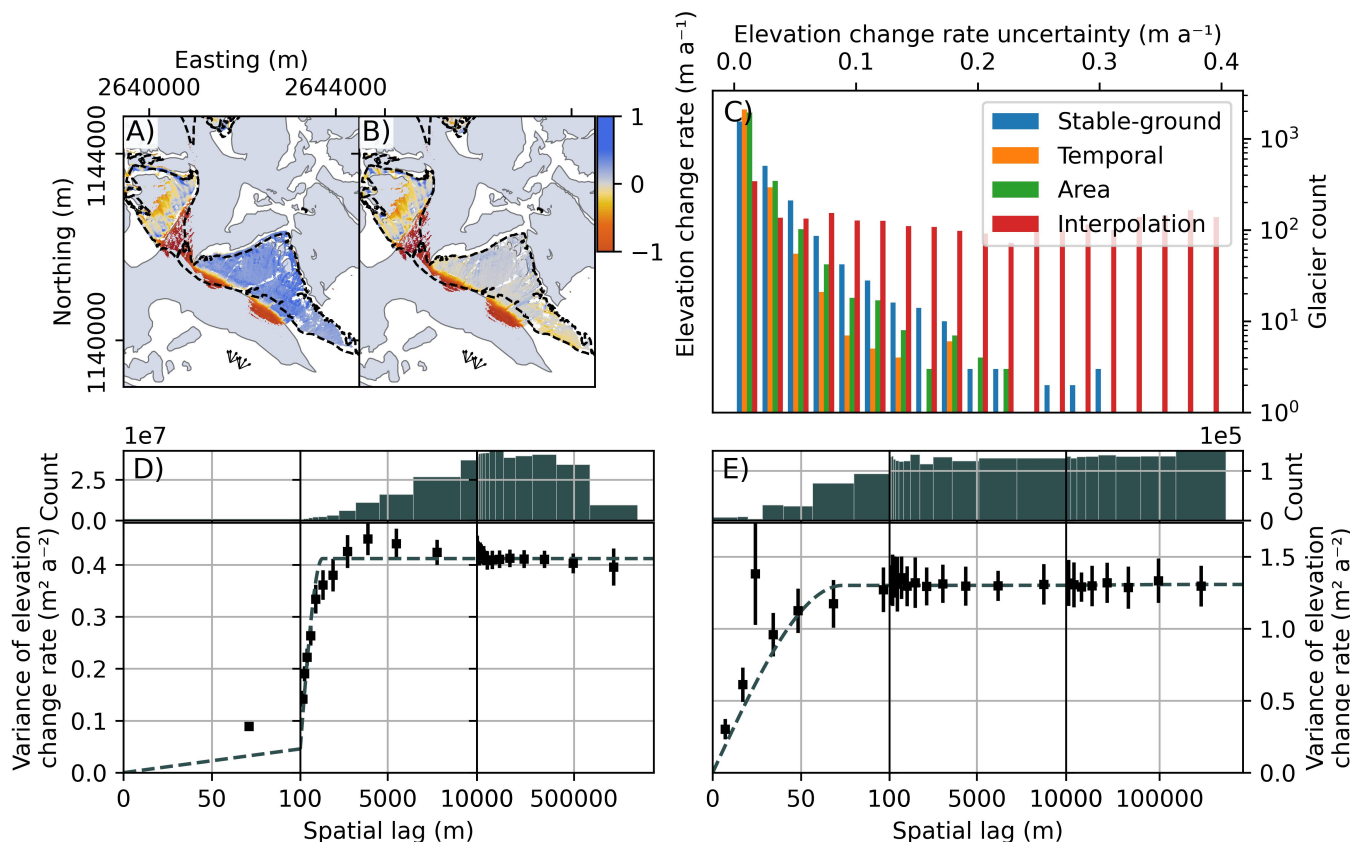


Figure 4. Error figure ensemble. **A+B**) Differences of an individual DEM before (**A**) and after (**B**) coregistration. The arrows indicate the locations and directions of the images used for generating the ca. 1931 DEM. The dashed lines indicate the theoretical viewshed of the stereo-pair (pre-calculated by swisstopo). **C**) Histogram showing the magnitude of the different components for the elevation change uncertainty of each individual glacier. **D+E**) variograms of interpolated (**D**) and stable-terrain (**E**) elevation difference uncertainties, showing the variance of all pairs of pixels at a given distance (or lag) as a function of that lag. The individual markers show the empirically derived variance, their error bars show their 95% confidence intervals, and the dashed line shows the variogram model (sum of two spherical models). The histograms above the variograms show the pairwise sample count for each empirically derived variance marker.

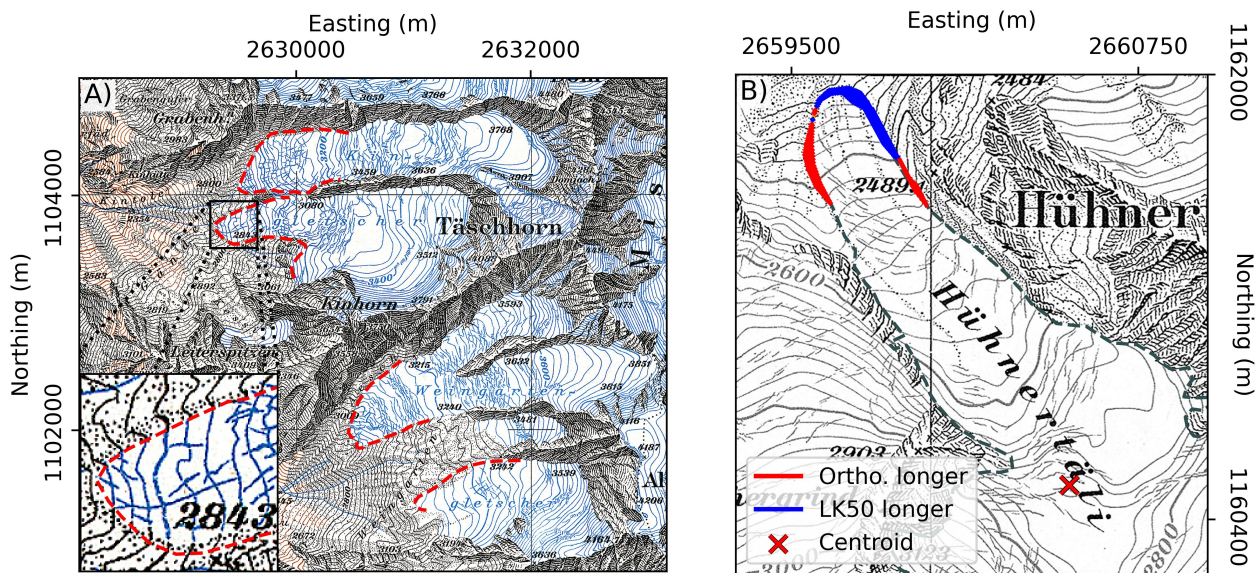


Figure 5. A) Glacier outlines drawn from orthoimages generated in this study (dashed red), superimposed on a sheet of the LK50 map series. B) Comparison between glacier outlines derived by digitizing the LK50 map series and orthoimages. Red shading indicates that the outline drawn from the orthoimage is farther away from the centroid than the outlines derived from the LK50 map series. Blue shading indicates that they are closer.

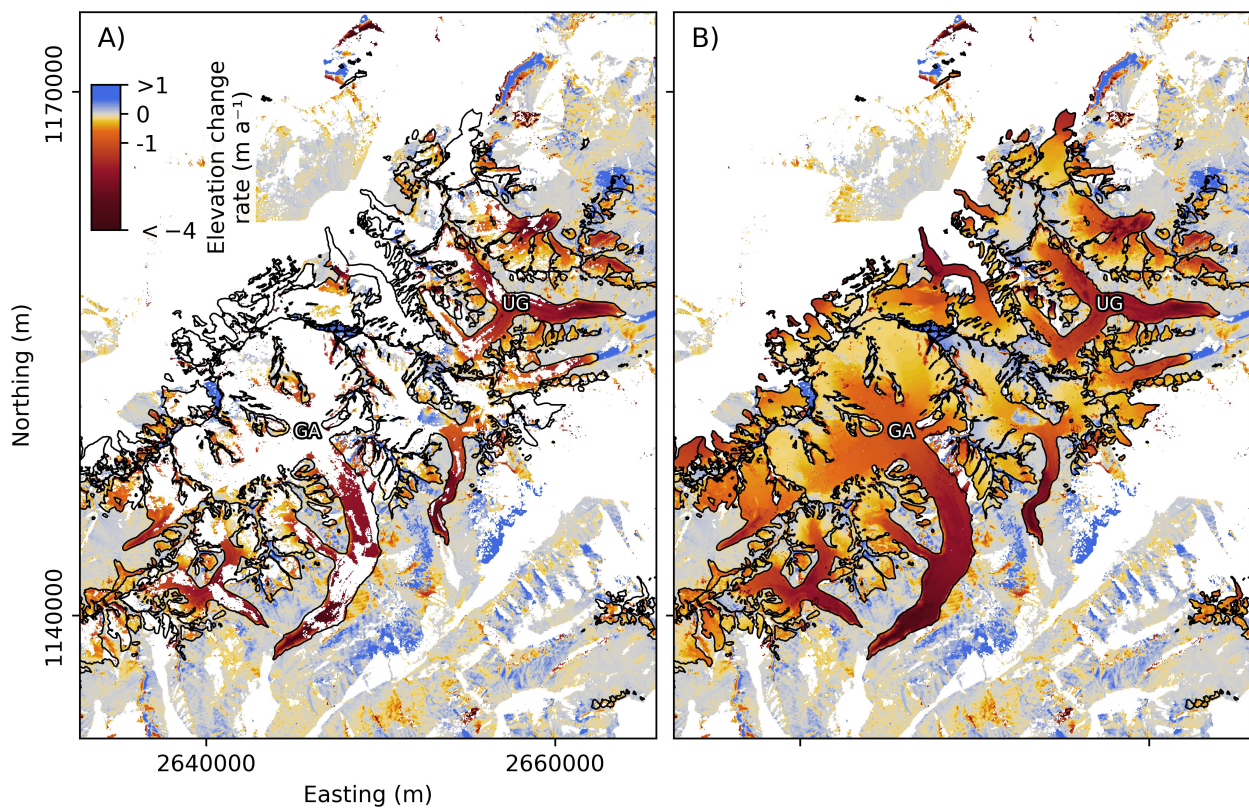


Figure 6. Maps of average ice thickness change rates ($dH dt^{-1}$) over the period 1931–2016 before (A) and after (B) interpolation. The area shows Grosser Aletschgletscher (GA), Unteraargletscher (UG) and other neighbouring glaciers. Glacier outlines from ca. 1931 are drawn in black.

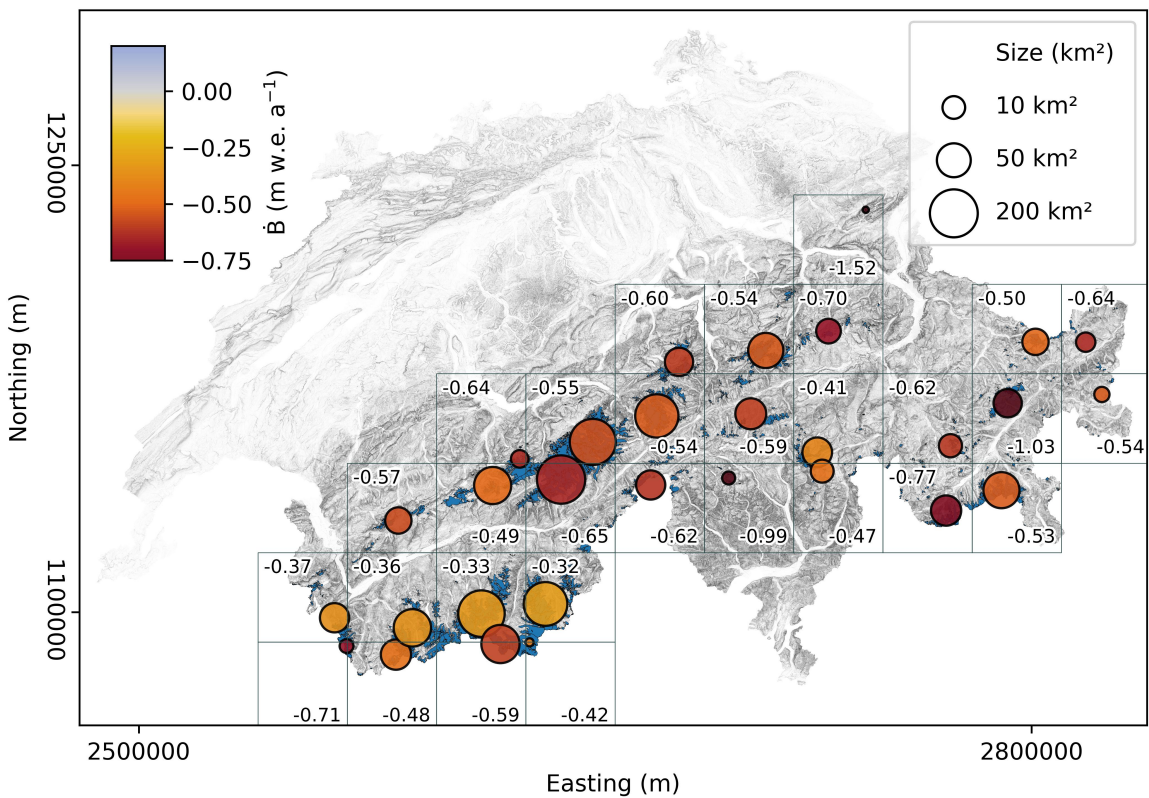


Figure 7. Area-weighted geodetic mass balance rates (colours and numbers) for 30 km×30 km tiles (grey squares). The location of each circle is the average glacier centroid weighted by area in the tile, and their sizes indicate the glacier area in ca. 1931.

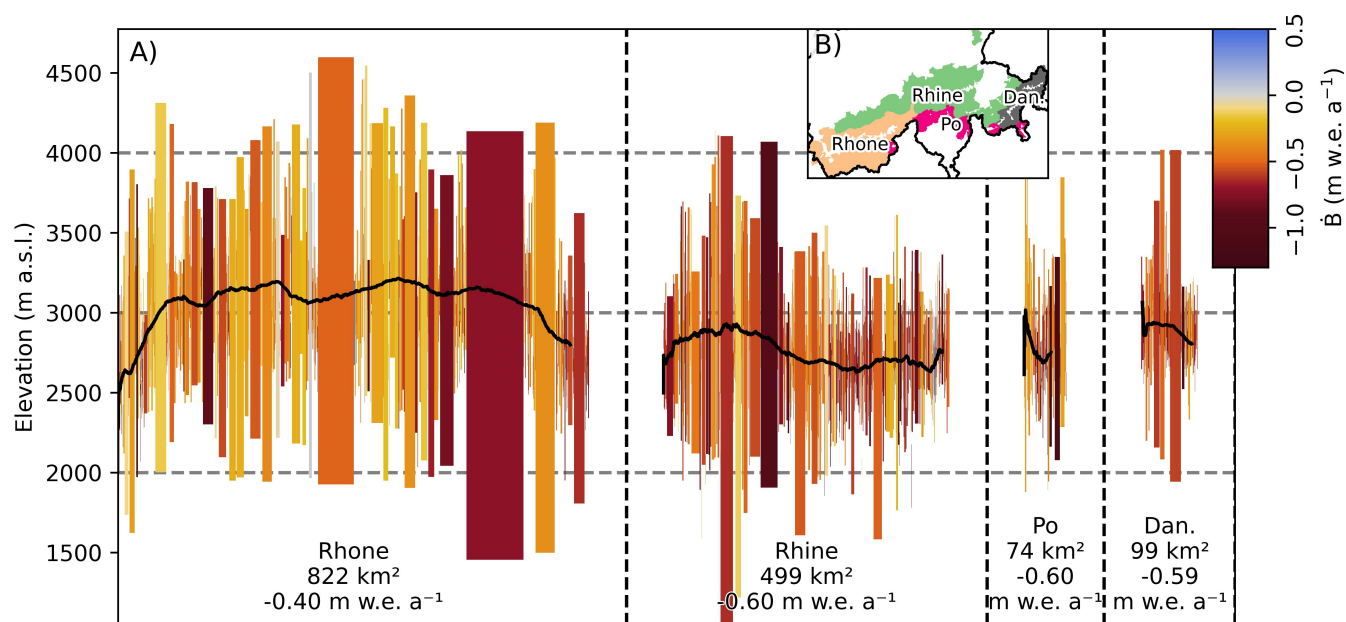


Figure 8. West-to-east transect of glaciers in Switzerland (A), grouped by the four main drainage basins (B). Each bar represents a glacier; the width indicates the ca. 1931 glacier area, the colour shows the average geodetic mass balance from 1931–2016, and the lower and upper bounds show the glacier’s modern elevation range. The near-horizontal black lines are moving averages of the median glacier elevations. For each drainage basin, the total area as of ca. 1931 is given, together with the average geodetic mass balance weighted by glacier area.

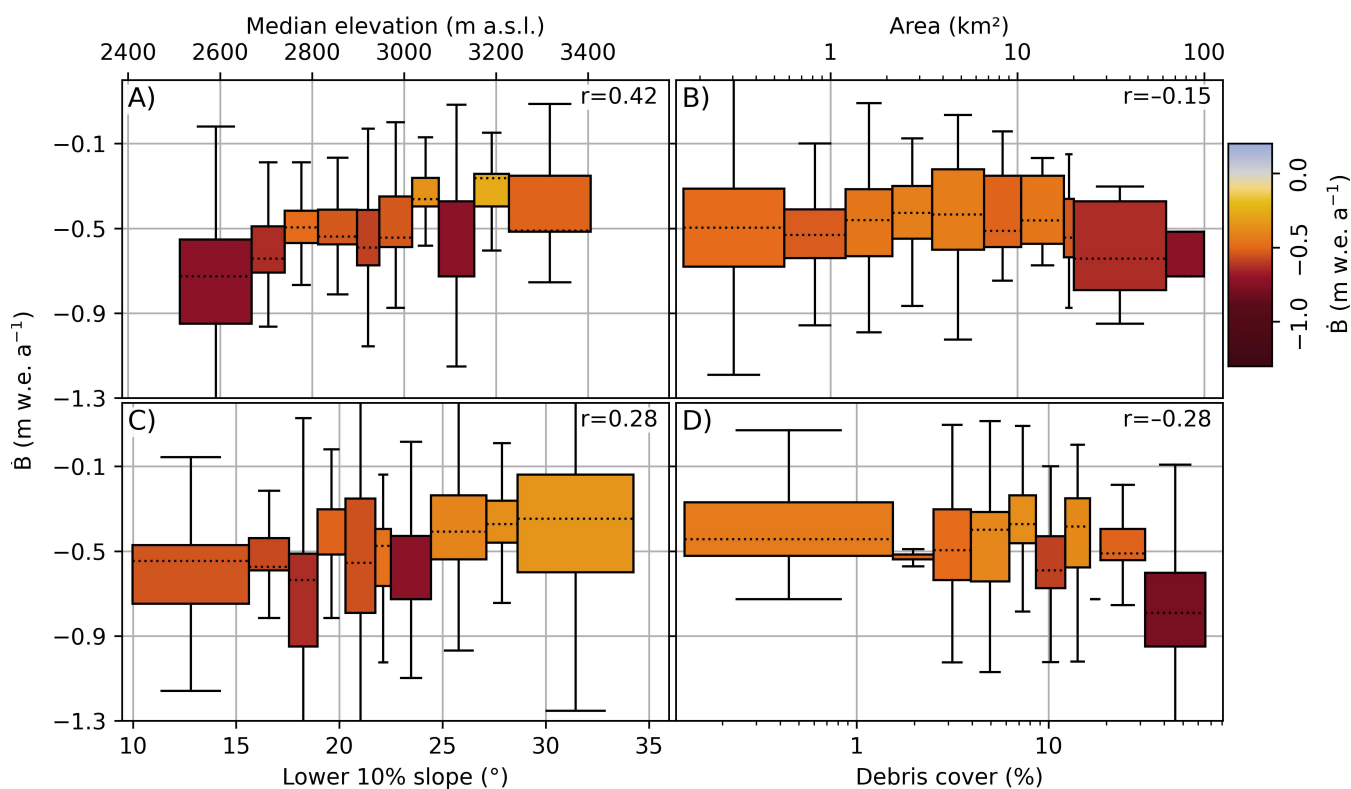


Figure 9. Area-weighted 10th percentile (0–10%, 10–20%, etc...) boxplots showing the relations between 1931–2016 average glacier mass change rates (vertical axes and colours) and different morphological parameters (horizontal axes). The whiskers extend from the box by $1.5 \times$ the inter-quartile range (IQR). The stated Pearson correlation coefficients (r) refer to the unbinned variables. **A)** Correlation with median glacier elevation, indicating that lower elevations show larger mass loss rates. **B)** Correlation with glacier area, showing no clear relation. **C)** Correlation with the slope of the lowermost 10% of the glacier surface, possibly showing higher mass change rates for glaciers with flatter termini. **D)** Correlation with fractional debris cover in 2016 (taken from Linsbauer et al., 2021), indicating that higher mass change rates may be found for glaciers with high debris-coverage percentage.

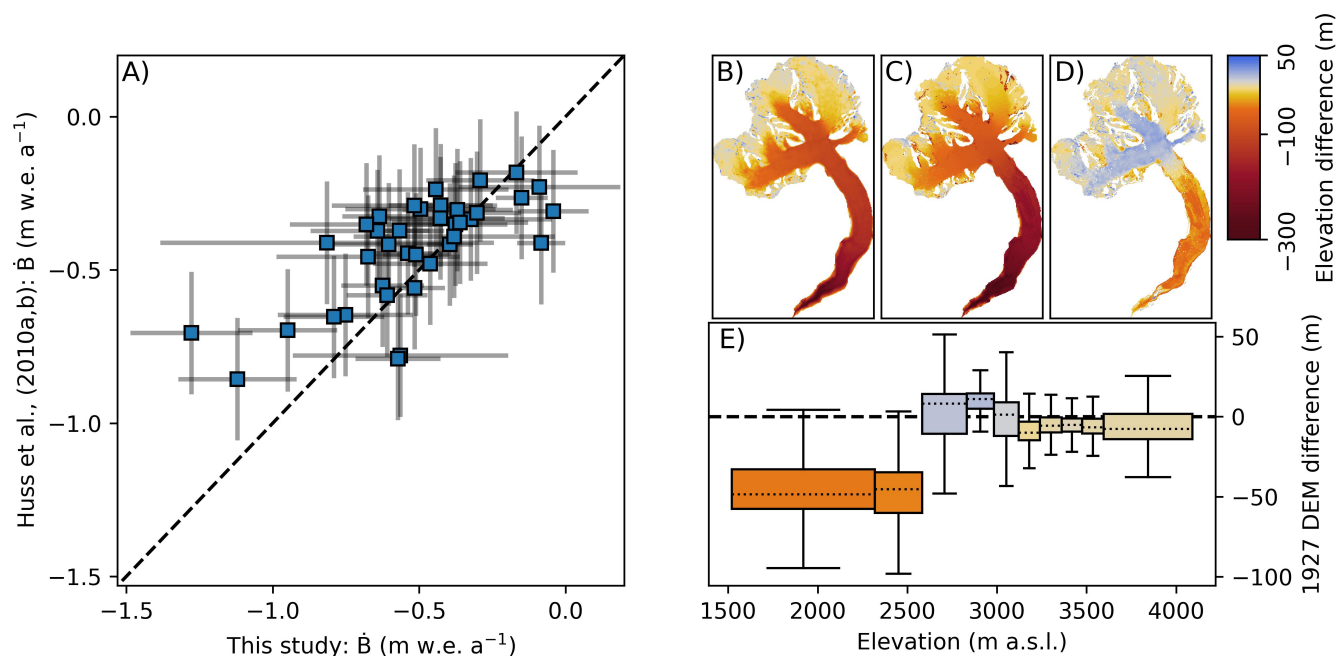


Figure 10. **A)** Comparison of 39 glacier-wide mass balances inferred in this study with mass balance derived from modelling, constrained by geodetic surveys at decadal intervals (blue squares; Huss et al., 2010a, c). The Pearson correlation coefficient between the points is 0.71. The horizontal uncertainty bars are the 95% confidence intervals of this study, the vertical uncertainties are fixed uncertainties of 0.2 m w.e. a⁻¹ (see Sec. 5.1), and the dashed line is a 1:1 line. **B)** Elevation difference between the 1927 topographic map digitized and used by Bauder et al. (2007), and the SwissALTI3D DEM in 2017. **C)** Elevation difference between the DEM mosaic generated in this study and the SwissALTI3D DEM in 2017. **D)** Difference between the 1927 topographic map and the DEM mosaic from this study (map – this study). **E)** Differences between the two 1927 DEMs (c.f. **D**) binned for every 10th percentile of elevation. A general agreement is seen on the upper part of the glacier (above ~2700 m a.s.l.), but the tongue is portrayed as smaller in the topographic map.